Liu et al. *NPG Asia Materials* (2018) 10: 293–308
DOI 10.1038/s41427-018-0029-2

NPG Asia Materials

ARTICLE Open Access

A highly sensitive and moisture-resistant gas sensor for diabetes diagnosis with Pt@In_2O_3 nanowires and a molecular sieve for protection

Wei Liu[1], Lin Xu[1], Kuang Sheng[1], Xiangyu Zhou[1], Biao Dong[1], Geyu Lu[1] and Hongwei Song[1]

Abstract

Sensitive and selective detection of acetone in human exhaled breath plays an important role in the diagnosis of diabetes. However, obtaining a reliable response to ppb levels of acetone and avoiding cross-sensitivity due to the large amount of moisture in exhaled breath are still great challenges. In this work, a type of acetone sensor with ultrahigh sensitivity and moisture resistance is reported. Electrospun In_2O_3 nanowires with a controllable Pt core (Pt@In_2O_3 core-shell nanowires) are designed and prepared as sensitive layers. A mesoporous silica molecular sieve is further integrated as the moisture filter layer. The Pt@In_2O_3 core-shell nanowire-based sensor exhibits a highly improved response compared with a sensor based on pure In_2O_3 nanowires due to the probable increase in surface resistance and the introduction of p–n junctions after rational design of the structure. In addition, a good performance in terms of the fast dynamic process, selectivity and long-term stability is also achieved, and the detection limit can be as low as 10 ppb, which is much lower than the concentration level of 1.8 ppm in the exhaled breath of diabetic patients. The influence of the large amount of moisture is greatly weakened by using the molecular sieve as a moisture filter layer, leading to much improved sensitivity in clinical sample detection among healthy and diabetic patients. Based on the optimized composite structure of the Pt@In_2O_3 core-shell nanowire sensor and moisture filter layer, a simple portable sensing prototype is successfully fabricated. The reported Pt@In_2O_3 core-shell nanowires and the acetone sensing approach open up a new opportunity for a simple, inexpensive, and noninvasive diagnosis of diabetes.

Introduction

Diabetes is a global chronic disease arising from metabolic disturbances[1]. Traditional methods for conducting blood glucose measurements during both hospital examinations and in-home care are invasive, which undoubtedly causes patients to undergo additional psychological stress and pain[2]. It is reported that diabetes can also be reflected by a biomarker in human breath, i.e., gaseous acetone, and that an exhaled concentration of acetone in excess of 1.8 ppm generally implies a high diabetes risk due to glucose metabolism and carbohydrate digestion in the human body[3]. Therefore, accurate and selective detection of sub-ppm levels of acetone biomarkers in breath is considered a promising diagnostic tool for performing a noninvasive health check.

The semiconductor oxide (SMO)-based gas sensor is one of the most promising devices for practical detection related to, for example, personal health[4], air pollution[5], and safety protection areas[6] due to its key advantages in terms of high sensitivity, fast response and recovery dynamics, ease of operation and low cost[7,8]. One potential

Correspondence: Lin Xu (linxu@jlu.edu.cn) or Hongwei Song (songhw@jlu.edu.cn)
[1]State Key Laboratory of Integrated Optoelectronics, College of Electronic Science and Engineering, Jilin University, Changchun 130012, People's Republic of China

application of the SMO-based sensor is the detection of biomarker molecules in exhaled breath to distinguish between healthy people and those suffering from a variety of diseases[9,10]. However, some obstacles remain regarding the practical application of this kind of sensor. First, the current developed sensing materials can hardly satisfy the requirements of high sensitivity and low detection limit to trace acetone in exhaled breath[11,12]. For n-type SMO-based gas sensors, the sensing mechanism is mainly based on the surface chemical redox reactions that occur between surface absorbed oxygen ions and target gases, which will change the amount of electrons in n-type SMOs and thus change the corresponding resistance. One key method for significantly improving the sensing performance is to introduce noble metal catalytic additives into the nanostructured SMOs to sensitize the corresponding reactions[13]. However, because of the increased mobility of metal nanoparticles on the substrates at higher temperatures, noble metal nanoparticles are not stable to heating, which results in a loss of catalytic activity[14]. In addition, noble metal nanoparticles can be poisoned by many chemicals, such as H_2S, SO_2, and thiols, thereby further decreasing the performance of the sensor[15]. Heterostructures with metal cores and semiconductor shells are thus the strongest candidates for high-performance gas sensors due to the controllable chemical and thermal stability of the metal cores, and the charge transfer between the metal cores and semiconductor shells. In addition, by controlling the surface absorption mechanism, the n-type reaction mainly occurs on or near the surface. Regarding the metal core@SMO shell structure, the metal core can effectively help not only increase the conductivity but also catalyze the reaction.

Second, the large amount of moisture that exists in exhaled breath severely interferes with acetone detection. Many attempts at eliminating the humidity effect have been made. For example, Haick et al.[16] introduced humidity compensation and cross-reactive array methods, which can yield more accurate target gas values at various humidity levels (up to approximately 80% relative humidity, RH)[17]. Both Nishibori and Mondal et al.[18,19] added some extra dehydrating components to decrease the influence of the humidity. However, these methods also have many side-effects, resulting in sensing devices that are much larger and/or more complicated.

To solve these problems, we successfully fabricated Pt@In_2O_3 core-shell nanowires (NWs) that are ultrasensitive to acetone via a simple co-electrospinning method. This kind of one-dimensional (1D) NWs not only possesses a highly active surface area for acetone recognition, but also has very good electron transmission ability due to the continuous Pt core. Moreover, an SBA-15 molecular sieve containing two-dimensional hexagonal channels was further introduced as an effective moisture filter on top of the sensitive layer; this sieve can effectively maintain the advantage of nanodevices, namely, their miniaturized scale[20]. The as-designed devices were successfully used to detect trace acetone in exhaled breath, making it possible to accurately distinguish healthy people from individuals with diabetes based on clinical samples. Moreover, according to the corresponding analysis results, the introduction of the SBA-15 molecular sieve layer can effectively protect the sensor from the influence of high humidity. This sensor is highly promising for the high-performance diagnosis of diabetes in a noninvasive manner.

Materials and methods

Materials

Indium nitrate ($In(NO_3)_3.4.5H_2O$, 99.5%) was purchased from Sinopharm Group, China. Polyvinylpyrrolidone (PVP, Mw ~ 1,300,000 g mol^{-1}), polyacrylonitrile (PAN, Mw ~ 1,500,000 g mol^{-1}), and chloroplatinic acid (H_2PtCl_6) were purchased from Sigma-Aldrich. N,N-dimethylformamide (DMF, 99.5%), ethanol (99.9%), and acetone (99.9%) were purchased from Sinopharm Group. All reagents were analytical grade and used as purchased without further purification. The SBA-15 molar sieve was obtained from Jiaxing New Materials Company, China. Detailed information regarding SBA-15 is listed in Supplementary Table S1.

Preparation of In_2O_3 NWs with a continuous Pt core

In this study, a simple one-step co-electrospinning method was used for the fabrication of Pt@In_2O_3 core-shell NWs with different morphologies. In a typical procedure, 0.72 g of $In(NO_3)_3.4.5H_2O$ was dissolved in 10 mL of a solution of DMF and absolute ethanol (v:v = 4:1) and then magnetically stirred at room temperature. After 30 min, 2 g of PVP was added to the mixture to ensure that the weight ratio of $In(NO_3)_3$ to PVP equals 0.36. Finally, the homogeneous shell precursor solution was obtained after 6 h of continuous stirring. For preparation of the inner precursor solution for co-electrospinning, different amounts of H_2PtCl_6 (50, 100, and 200 μL) were dissolved in 10 mL of DMF solution to obtain In/Pt atomic ratios of 20, 10, and 5, respectively. After stirring for 30 min at room temperature, 1 g of PAN was added to the corresponding solutions, which were then vigorously stirred for 6 h. Finally, different transparent yellow precursor solutions were obtained. Then, the as-prepared precursor solutions were loaded into plastic syringes, which were fixed 15 cm above a grounded collector for co-electrospinning. A voltage of 15 kV generated by a high-voltage DC power supply was applied to the tip of a stainless steel concentric needle connected to each syringe. The flow rates of the core-shell NWs were adjusted to 3 and 5 μL min^{-1} for the core and shell layers,

respectively. Then, the as-spun fiber mats were collected and put into a tube furnace, the temperature inside which was increased at a rate of 1 °C min^{-1} from room temperature to 500 °C and then kept at that temperature for 3 h to ensure the complete removal of carbon residues and the crystallization of inorganic products. The pure In_2O_3 NWs sample was spun using the shell precursor solution at a flow rate of 3 μL min^{-1}, and Pt/In_2O_3 mixed NWs were obtained by mixing the shell precursor solution with 100 μL of H_2PtCl_6 at a flow rate of 3 μL min^{-1}. The corresponding details are given in the Supporting Information.

Fabrication and measurement of gas sensors

In a typical process, a ceramic tube substrate with a pair of Au electrodes on its top surface was used. The as-obtained NW pastes (weight ratios of samples to ethanol were 5:1) were coated onto the ceramic tube substrate to form sensing layers and then sintered at 350 °C for 3 h to increase the stability. After sintering, the gas sensors were thermally aged using aging equipment at a heating voltage of 5 V for 48 h before taking the first measurement. The gas sensing properties were measured using a WS-30 gas sensing system (Weisheng Instruments Company, Zhengzhou, China) under laboratory conditions (22 ± 2 RH%, 20 ± 2 °C). The details regarding the process of measuring the gas sensing behaviors were given in our previous work[21]. The response of the sensor was determined as the resistance ratio of the sensor resistance in air (R_a) to its resistance in the target gas (R_g). The response and recovery times (τ_{res} and τ_{rec}, respectively) were defined as the times required to reach 90% of the total resistance change in the tested gas and air. A static process was used to achieve different gas concentrations of the target gases. More specifically, the gas source was 200 ppm standard gas mixed with N_2. A certain amount of standard gas, which had been pumped in a vacuum and then mixed with atmospheric gas, was injected into a glass chamber with a small mouth (approximately 2.5 L in volume). Both the inner wall of the mouth and the corresponding rubber stopper were sealed using petroleum jelly to maintain the stability of the gas concentration. When testing, a sensor with an extended line passing through the rubber stopper was put into the chamber; when the response reached a constant value, the sensor was taken out to return the ambient air to its initial state.

To fabricate the moisture filter layer, a 56.7 mg mesoporous molecular sieve was thoroughly mixed with 1 mL of ethanol by grinding to form a homogeneous slurry. Then, the as-obtained slurry was coated onto the outer surface of the as-obtained gas sensor by slowly pulling the sensor out at a rate of 0.1 cm s^{-1}. Finally, the obtained gas sensor was sintered at 200 °C for 1 h to increase the stability.

Collection of breath samples

Breath samples were collected from diabetic volunteers at the First Hospital of Jilin University and health volunteers at the State Key Laboratory of Integrated Optoelectronics of China. The statistics of the tested volunteers, including their age, gender, and diabetes type, are summarized in Supplementary Table S2. All volunteers were asked to not eat anything after their meals for 2 h and to rinse their mouths with water three times (10 min before testing). These clinical samples were collected inside gas collection bags (1 L) with an aluminum coating (De Lin Instrument Company, Dalian) and stored in a suitable environment until analysis. The collection process is shown in Supplementary Fig. S1. Finally, the samples were injected into the sensing measurement system using a diaphragm pump.

Portable sensing device for diabetes

We designed a simple portable sensing device for real-time detection, the system languages of which are Chinese and English. In the portable sensing device, S is defined as the real-time response value, and S_m is the response value of the last measurement. The detailed testing results are shown in Supplementary Information Video 1 (in Chinese) and Video 2 (in English).

Results and discussion

A schematic illustration of the process of producing the Pt@In_2O_3 core-shell NWs is shown in Fig. 1a (the process is described in detail in the experimental section). First, the morphologies of the as-prepared Pt@In_2O_3 core-shell NWs as well as pure In_2O_3 and Pt/In_2O_3 NWs were studied using a scanning electron microscope (SEM). As shown in Fig. 1b, the pure In_2O_3 NWs exhibit a uniform diameter distributed in the range of 65–85 nm (Supplementary Fig. S2a) and a rough surface with some mesopores, which is consistent with our previous study[22]. The morphology of the Pt/In_2O_3 mixed NWs (Fig. 1c) is different from that of the pure NWs. A hierarchical structure with the NWs as the trunk (~ 75 nm, Supplementary Fig. S2c) can be found, and the surface is decorated with several nanoparticles (~ 42 nm, Supplementary Fig. S2b). The Pt@In_2O_3 core-shell NW outer surface morphologies show similarities with those of the pure In_2O_3 NWs (Fig. 1d–f). The diameter becomes more uniform as the amount of Pt in the core increases, and the average diameters of the Pt@In_2O_3 core-shell NWs with In/Pt atomic ratios of 20, 10, and 5 are ~ 74, 80, and 98 nm, respectively, (Supplementary Fig. S2d–f). Note that the pure In_2O_3 NWs and Pt/In_2O_3 mixed NWs are denoted by S1 and S2 and that the Pt@In_2O_3 core-shell NWs with In/Pt atomic ratios of 20, 10, and 5 are denoted by S3, S4, and S5, respectively, for convenience.

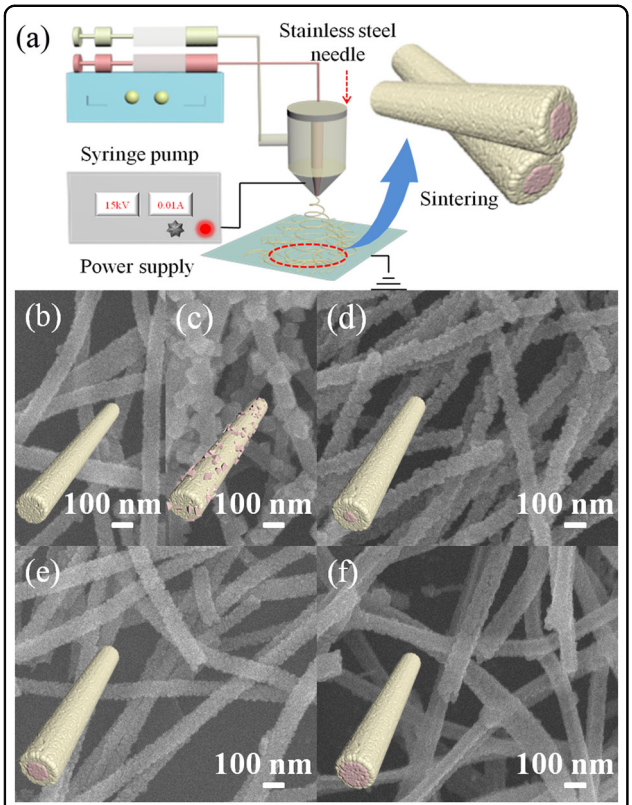

Fig. 1 **a** Schematic illustration of the electrospinning fabrication process for Pt@In_2O_3 core-shell NWs. SEM images of the **b** S1, **c** S2, **d** S3, **e** S4, and **f** S5 NWs

To obtain detailed information regarding the microstructures and morphologies of the as-prepared samples, transmission electron microscopy (TEM) images of different NW samples are further examined. As shown in Fig. 2, the TEM images of pure In_2O_3 NWs and Pt/In_2O_3 mixed NWs are similar to the corresponding SEM images. In the TEM image of In_2O_3 NWs (Fig. 2a), the porous structure of the NWs can be distinguished more clearly, which is beneficial to the interaction between the NWs and gas molecules in the subsequent sensing process. For the Pt/In_2O_3 mixed NWs, the specific hierarchical structure can be further confirmed based on the corresponding TEM (Fig. 2b) and energy dispersive X-ray mapping (EDX, Supplementary Fig. S3) images. In contrast to the SEM images, the core-shell structure can be clearly observed in the TEM image of the Pt@In_2O_3 core-shell NWs. Regarding the S3 Pt@In_2O_3 core-shell NWs (Fig. 2c), the inner Pt core comprises some discontinuous parts instead of being an intact NW core due to the low Pt core content in the precursor solution (50 μL in 10 mL of DMF). When the concentration of H_2PtCl_6 in the DMF is increased to 100 μL (S4 Pt@In_2O_3 core-shell NWs), a good core-shell structure can be obtained. As indicated in Fig. 2d, a long and continuous core structure with an average diameter of 27 nm exists. After further increasing the concentration to 200 μL, the core diameter increases to 86 nm, while the thickness of the outer In_2O_3 shell is only several nanometers (Fig. 2e). Meanwhile, the wall thickness of the outer In_2O_3 shell (Supplementary Fig. S2g–i) and the corresponding grain sizes of In_2O_3 (Supplementary Fig. S4) are also measured based on the TEM images. The average wall thicknesses of the outer In_2O_3 shell are 25, 27, and 7 nm for the Pt@In_2O_3 core-shell NWs, and the average grain sizes for NW samples S1–S5 are, 10, 7, 21, 17, and 16 nm, respectively. The estimated grain size of the Pt/In_2O_3 mixed NWs (7 nm) is smaller than that of the In_2O_3 NWs (10 nm). Similar results were previously observed for noble metal-loaded SMO NWs made via electrospinning[23,24], which implies that noble metal can prevent the grain growth of SMO particles. For the Pt@In_2O_3 core-shell NWs, all the grain sizes of the In_2O_3 shell increase with increasing Pt loading (Fig. 2c–e). According to classical grain growth theory, the grain growth rate of the In_2O_3 shell is strongly dependent on the differences in grain radius and disorientation angles in the surrounding grains[25]. For the grains in the outer layer of the core-shell structure, further grain growth becomes easier due to the random orientations of the surrounding grains. Therefore, the grain sizes can grow further in the shell region. For the S3 Pt@In_2O_3 core-shell NWs, the grain size is the largest one. This result may be related to the insufficient amount of Pt in the core, which makes the grain size of the In_2O_3 shell in the inner part less restricted by the small disorientations of the inner Pt core, thereby leading to a larger grain size.

Figure 2f shows a high-resolution TEM (HRTEM) image of the S4 Pt@In_2O_3 core-shell NW sample; a uniform lattice fringe can be observed over an entire primary particle. The lattice fringes with $d = 0.292$ nm (222) and 0.506 nm (200) coincide well with the crystallographic planes of body-cubic In_2O_3. The lattice fringes with $d =$ 0.192 nm (111) coincide well with the crystallographic planes of cubic Pt. In addition, selective area electron diffraction (SAED) patterns are examined for each NW, as shown in the insets of the corresponding panels. All five NWs exhibit a polycrystalline In_2O_3 structure with interplanar spacings of (200), (222), (400), (440), and (622), consistent with the cubic crystal structure. The Pt core also exhibits a (111) crystallographic plane resulting from the cubic Pt. To further determine the specific distribution of O, In, and Pt elements, EDX mappings of the S4 Pt@In_2O_3 core-shell NW sample are conducted using a scanning transmission electron microscope (STEM, Fig. 2g). As shown in Fig. 2h, i, the distributions of O and In elements are similar and overlapping and are mainly homogeneously distributed over the shell of the NWs, while the Pt element is concentrated in the core of the

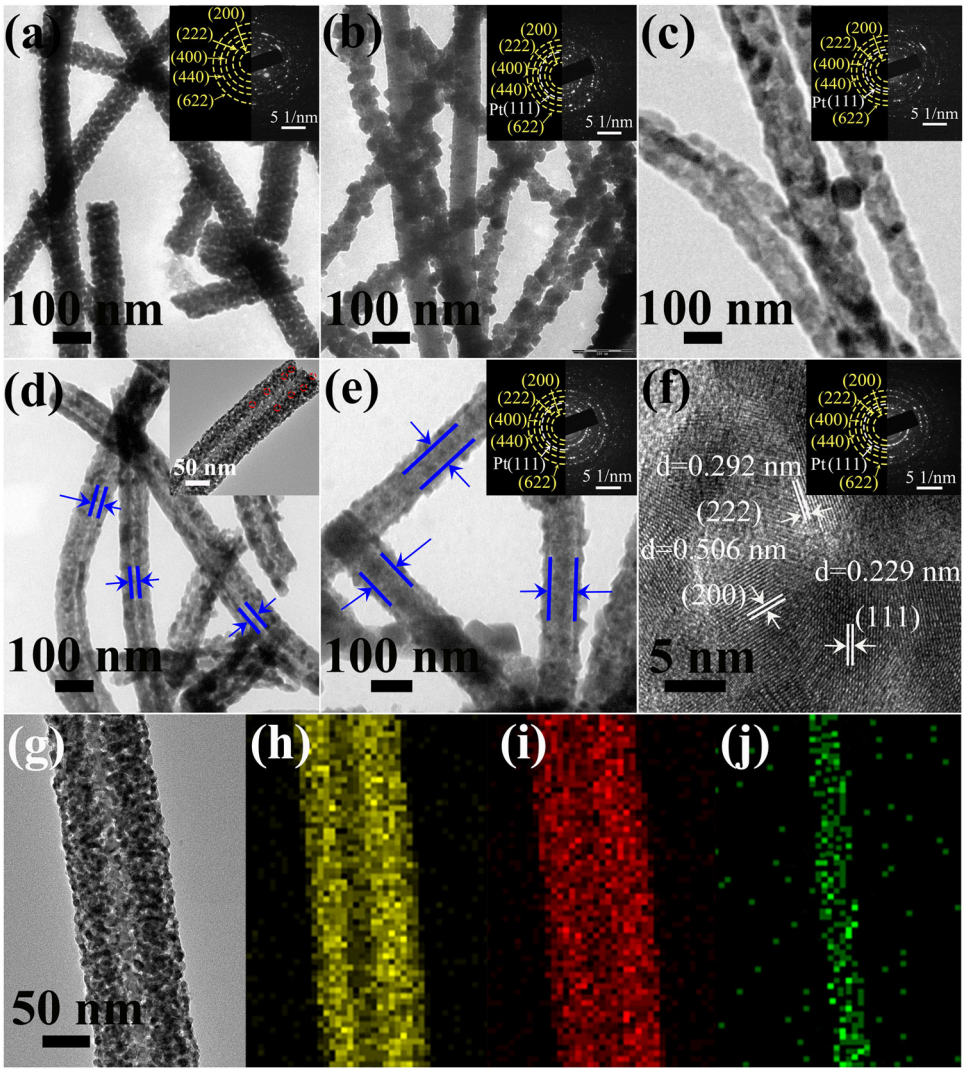

Fig. 2 TEM images of the **a** S1, **b** S2, **c** S3, **d** S4, and **e** S5 NWs, and **f** HRTEM of S4. The insets in panels **a**–**c**, **e**, and **f** are the corresponding SAED patterns, the inset in panels **d** is the enlargement of the image of S4. **g** STEM images of the S4 Pt@In_2O_3 core-shell NW sample and EDX elemental mapping images of **h** O, **i** In, and **j** Pt in the S4 Pt@In_2O_3 core-shell NW sample

core-shell NWs (Fig. 2j). These results indicate that the Pt@In_2O_3 core-shell NWs were successfully obtained.

Supplementary Fig. S5 shows the X-ray diffraction (XRD) patterns of the as-prepared NWs. For the pure In_2O_3 NWs (S1), the corresponding diffraction peaks are very consistent with the standard XRD card of cubic In_2O_3 (JCPDS 06-0416), and no trace of any other phases can be detected. After the introduction of Pt, obvious diffraction peaks of body-centered cubic Pt (JCPDS 65-6828) can be observed (S2 to S5). This is consistent with the results from the HRTEM and SAED characterization. In addition, as the amount of Pt in the Pt@In_2O_3 core-shell NWs (S3 to S5) increases, the corresponding peak intensity of Pt increases accordingly.

The valence chemistry and binding energy of the constituent elements are further demonstrated via X-ray photoelectron spectroscopy (XPS) analysis, as shown in Fig. 3. The survey spectra of the NWs further confirm the presence of In, O, and/or Pt elements (Fig. 3a). As the number of different components changes in the composites, the intensities of the S1 to S5 characteristic peaks also change according to the same trends. The XPS spectra indicate that the atomic ratios of In/Pt for S1–S5 can be quantitatively calculated as 0, 9.8, 20.3, 9.7, and 5.2, respectively. This result is highly consistent with the initial concentration of the regent. According to the enlarged O 1s spectra (Fig. 3b), the O 1s core level electrons of all the as-prepared samples can be deconvoluted

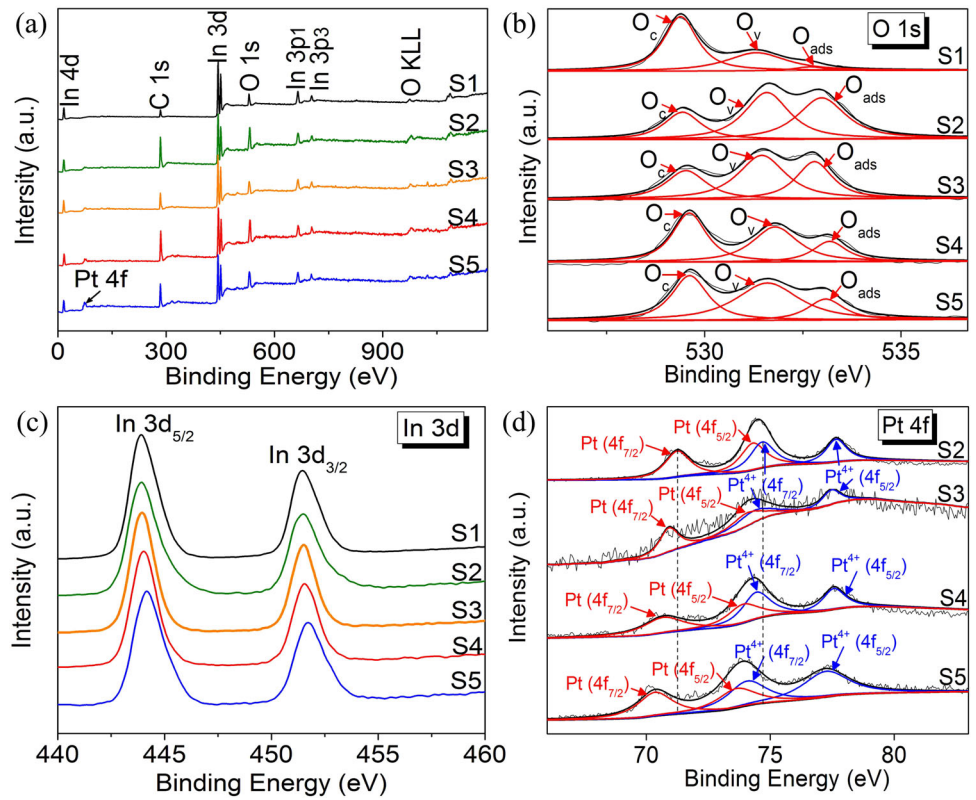

Fig. 3 a Survey, **b** O 1 s, and **c** In 3d high-resolution XPS spectra of the S1–S5 NW samples and **d** Pt 4 f high-resolution XPS spectra of the S2–S5 NW samples

into three peaks from low to high binding energy: crystal lattice oxygen (O_c), deficient oxygen (O_v), and adsorbed oxygen (O_{ads}) species or OH groups. The exact binding energies of the decomposition peaks in each NW sample are summarized in Supplementary Table S3. Note that the corresponding position of each sample is slightly different due to the different local surroundings. Herein, the deficient oxygen ratios of all the NWs are calculated using the ratio of the integral area of the deficient oxygen peak to the whole area of the O 1s peak. The corresponding deficient oxygen ratios are calculated to be 33.4%, 40.6%, 44.7%, 50.1%, and 39.5% for samples S1–S5, respectively. It is clear that the amount of deficient oxygen after introducing Pt (both in the core-shell and mixed cases) is much higher than that in the pure In_2O_3 NWs; moreover, the amount of deficient oxygen in the core-shell NWs is higher than that in the mixed case (except for S5).

High-resolution XPS spectra of the In 3d binding energy region are shown in Fig. 3c. The binding energies of In $3d_{5/2}$ and In $3d_{3/2}$ in the pure In_2O_3 NWs are determined to be approximately 443.9 and 451.5 eV, respectively. Compared to that of the pure In_2O_3 NW sample, the spectrum of the S2 sample (Pt/In_2O_3 mixed NWs) shifts slightly to a higher binding energy. The corresponding offsets of samples S3 to S5 are larger than the mixed one, even though they have a smaller or the same amount of Pt in the cases of the S3 or S4 Pt@In_2O_3 core-shell NWs. In addition, in Pt@In_2O_3 core-shell NW samples S3 to S5, the spectra also gradually shift to high binding energies as the amount of Pt in the core increases. Figure 3d shows the XPS spectra of Pt 4 f, which can be deconvoluted into two doublets. Taking the S3 Pt@In_2O_3 core-shell NW sample as an example, the doublet decomposition peaks at 70.2 and 73.5 eV can be assigned to metallic Pt, and the doublet decomposition peaks at 73.9 and 77.2 eV to oxidized Pt (Pt^{4+})[26,27]. The spin-orbit coupling energy between Pt $4f_{5/2}$ and $4f_{7/2}$ is 3.3 eV, which is consistent with a previous study[28]. On the other hand, the spectra for NW samples S2 to S5 gradually shift to lower binding energies. Generally, the shift of binding energies in XPS spectra can be explained by the electron transfer due to the strong interactions between or the different electronegativities of the corresponding metal ions[29,30]. From the perspective of electronegativity, the electronegativities of the In^{3+} ion and Pt atom are approximately 1.78 and 2.28, respectively[31,32]. The Pt atom, with its larger electronegativity, can draw electrons from the In^{3+} ions, leading to the number of electrons decreasing for the In^{3+} ions but increasing for the Pt atom due to the screening effect. As a consequence, the Pt 4 f peaks shift toward a lower

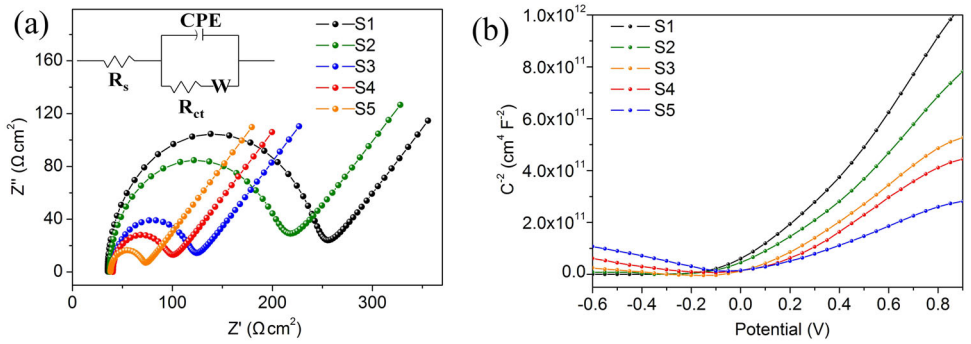

Fig. 4 a EIS Nyquist plots of S1–S5 NW sample-based electrodes with a frequency range of 0.1 Hz to 100 KHz and **b** Mott–Schottky plots of the S1–S5 NW samples at 1 KHz

binding energy, while the In 3p peaks shift toward a higher binding energy, increasing the activity of the surface In_2O_3.

To understand the electrical properties of the as-prepared NWs, electrochemical impedance spectroscopy (EIS) and Mott–Schottky curves are studied. Figure 4a shows the Nyquist plots of different samples. The corresponding curves are fitted using circuit elements consisting of one resistor and one RCW circuit. The corresponding equivalent circuit is shown in the inset, and the corresponding fitted data are listed in Supplementary Table S4. In our case, R_s represents the diffusive resistance of the electrolyte in electrode pores and the proton diffusion in the host materials, which do not exhibit an obvious difference since we used the same supporting electrolyte for EIS measurements[33]. CPE, R_{ct}, and W are the film capacitance, charge transfer resistance, and Warburg impedance, respectively[34]. It can be clearly observed in both Fig. 4a and Supplementary Table S4 that the R_{ct} values have the following relationship: R_{ct} (S1) > R_{ct} (S2) > R_{ct} (S3) > R_{ct} (S4) > R_{ct} (S5). In other words, the conductivity of the NWs is improved after mixing with Pt compared to that of the pure In_2O_3 NWs, especially in the case of the Pt@In_2O_3 core-shell NWs (S3 to S5), indicating that the core-shell structure can effectively enhance the electron transfer process. Note that the R_{ct} value of the S4 Pt@In_2O_3 core-shell NWs is much lower than that of the S2 Pt/In_2O_3 mixed NWs, even though they contain the same amount of Pt, demonstrating the advantage of this core-shell structure.

Mott–Schottky analysis using a mono-frequency capacitance–voltage (C–V) sweep was carried out to investigate the Schottky contacts in the semiconductor devices. The Mott–Schottky plots of the S1–S5 NW samples are created according to the following equation:[35]

$$\frac{1}{C^2} = \frac{2}{\varepsilon\varepsilon_0 e_0 N_D}\left(E - E_{FB} - \frac{kT}{e_0}\right)$$

where C is the space charge capacitance; ε and ε_0 are the permittivities of the electrode and free space, respectively; e_0 is the elementary charge; E is the applied potential; E_{FB} is the flat band potential; k is Boltzmann's constant; and T is the absolute temperature. As shown in Fig. 4b, for the pure In_2O_3 NWs (S1 sample), only Mott–Schottky plots with a positive slope are observed, which is a distinct characteristic of n-type semiconductors[36]. After the introduction of Pt material, the typical "V-shape" (negative slope in the low potential range and positive slope in the higher potential range) is observed in the Mott–Schottky plots for the S2–S5 NW samples, demonstrating that some p–n junctions were established[37,38]. As proved by the XPS results, the peaks of Pt^{4+} in the samples including Pt can be observed, indicating that a small amount of PtO_2 is formed. As already known, PtO_2 is a typical p-type material[39]; this means that p–n junctions formed between In_2O_3 and PtO_2. With the formation of the p–n junctions, the carrier densities of the S1–S5 NWs also increase remarkably. As shown in Fig. 4b, the Pt@In_2O_3 core-shell NWs exhibit smaller positive slopes than the Pt/In_2O_3 mixed NWs and pure In_2O_3 NWs, indicating that the introduction of a Pt core increases the carrier density of In_2O_3[31]. Moreover, this characteristic becomes more obvious with the increase in Pt in the S3–S5 Pt@In_2O_3 core-shell NW samples. This can be attributed to the greater amount of PtO_2 that exists between the interface of the Pt core and the In_2O_3 shell as the amount of Pt increases.

We have previously observed that In_2O_3 NWs exhibit good sensing behavior with respect to a low concentration of acetone gas[40,41]. With the introduction of a continuous Pt core, the Pt@In_2O_3 core-shell NW structures are expected to exhibit better sensing performances with respect to very low concentrations of acetone gas. Herein, the as-prepared NWs are used to fabricate sensors for the possible diagnosis of diabetes via exhaled breath. First, the optimum operating temperatures for each sensor are studied with respect to 10 ppm acetone gas. As shown in

Supplementary Fig. S6, the sensor based on S1 (pure In_2O_3 NWs) needs the highest operating temperature. After introducing Pt into In_2O_3, the operating temperatures of all sensors decrease due to the existence of more catalytically active center elements in the gas sensor, which is advantageous for carrier transport[42]. It should be mentioned that the way in which Pt is distributed has a great influence on the sensing properties in our case, even when the amount of Pt in the S2 and S4 NW sensors is the same. This indicates that a sensor with a core-shell structure not only exhibits a higher response value but also has a much lower operating temperature (320 °C). In addition, the different amounts of Pt in the core also result in different sensing performances. In the S3 Pt@In_2O_3 core-shell NW sensor, the insufficient amount of Pt hinders the formation of a completely continuous wire structure, which leads to a poor electron transfer ability. This prevents the sensor from reaching its optimal performance compared to the S4 Pt@In_2O_3 core-shell NW sensor. However, when the amount of Pt in the core is too high (S5 Pt@In_2O_3 core-shell NW sensor), the Pt core with a larger diameter will make the electron transfer occur too quickly and then deteriorate the sensing response, although it will have the lowest operating temperature.

Figure 5a shows the resistance response of different sensors when exposed to 1.8 ppm acetone. This acetone concentration level is important point, as it allows us to distinguish whether one person is at risk of diabetes based on their exhaled breath. All the sensors exhibit stable baselines in ambient air. They can quickly respond to the target gas and fully return to the baseline after being placed back into ambient air. Consistent with the result in Supplementary Fig. S6, the response of the S4 Pt@In_2O_3 core-shell NW sensor is the highest one, reaching 7 with respect to this dilute concentration, and the other sensors show the same change trends as those in Supplementary Fig. S6. Based on Fig. 5a, τ_{res} and τ_{rec} for NW sensors S1–S5 are further calculated and compared in Fig. 5b. τ_{res} and τ_{rec} show a decreasing trend from S1 to S5, and the S4 Pt@In_2O_3 core-shell NW sensor has the fastest dynamic process. Since the S4 Pt@In_2O_3 core-shell NW sensor has the best sensing performance, it is made the focus of further studies to obtain more information. Figure 5c exhibits the continuous dynamic response of the S4 Pt@In_2O_3 core-shell NW sensor to different concentrations of acetone (50 ppb–2 ppm; this range is around the health threshold of diabetes). As shown in the figure, the S4 Pt@In_2O_3 core-shell NW sensor has a very clear response of 1.9 to only 50 ppb of acetone, and as the concentration increases, the corresponding response also increases quickly. Moreover, the baseline is very stable after each cycle, indicating good real-time repeatability. The corresponding τ_{res} and τ_{rec} are also summarized and compared in Fig. 5d. As shown in the figure, the dynamic processes become shorter as the gas concentrations increase, which may occur because a lower gas concentration requires more time to reach equilibrium. The average τ_{res} and τ_{rec} are calculated to be 14 and 16 s, respectively, confirming the fast dynamic process of the S4 Pt@In_2O_3 core-shell NW sensor.

The steady-state responses of different sensors after 5 min of exposure to gaseous acetone as a function of acetone concentration from 10 ppb to 10 ppm are shown in Supplementary Fig. S7. The corresponding responses all show a linear increase in the study range, with the S4 Pt@In_2O_3 core-shell NW sensor exhibiting the best response. It shows a response up to 27 to 10 ppm of gaseous acetone, which is 2–6 times higher than that of the other sensors. According to the as-obtained linear equation, the detection limit of the S4 Pt@In_2O_3 core-shell NW sensor can be 10 ppb when $R_a/R_g \geq 1.2$ is used as the criterion for reliable gas sensing, which is much lower than that obtained in previous studies (Table 1). Table 1 lists the response, detection limit, testing ambience, τ_{res} and τ_{rec}, and operating temperature of some typical SMO-based acetone gas sensors along with the S4 Pt@In_2O_3 core-shell NWs considered in this work. As demonstrated by this table, the S4 Pt@In_2O_3 core-shell NW sensor offers a satisfactory performance compared to other acetone sensors, especially in terms of the detection limit and the response value under high humidity. The actual low detection limit (10 ppb) is also much lower than the limit for detecting diabetes and that of some previous studies, as listed in Table 1. In addition, the S4 Pt@In_2O_3 core-shell NW sensor yields very short τ_{res} and τ_{rec}. This confirms that the S4 Pt@In_2O_3 core-shell NWs may be a promising candidate for the monitoring of low-concentration acetone biomarkers in exhaled breath.

Selectivity is another important parameter for a gas sensor in practical use. Our work further tests various potential biomarkers in human breath, such as nitrogen dioxide for asthma[43], ammonia for kidney disease[44], and methanol and toluene for lung cancer[45]. The results are measured at the optimal operating temperatures of each sensor to evaluate the selective properties (Fig. 6a), and all the gas concentrations are 5 ppm. As clearly shown, the S4 Pt@In_2O_3 core-shell NW sensor exhibits high selectivity for gaseous acetone ($R_a/R_g = 14$ at 5 ppm) over other interfering analytes, to which it presents very low responses. The response to acetone is 5.1–10.2 times higher than that for other typical interfering gases. In addition, a cross-selectivity test of the S4 Pt@In_2O_3 core-shell NW gas sensor is conducted by testing the response to 5 ppm of some typical interfering gases when 5 ppm of acetone is already present (Table 2). As shown, compared to the response to acetone by itself, the responses to acetone when other interfering gases appear change only

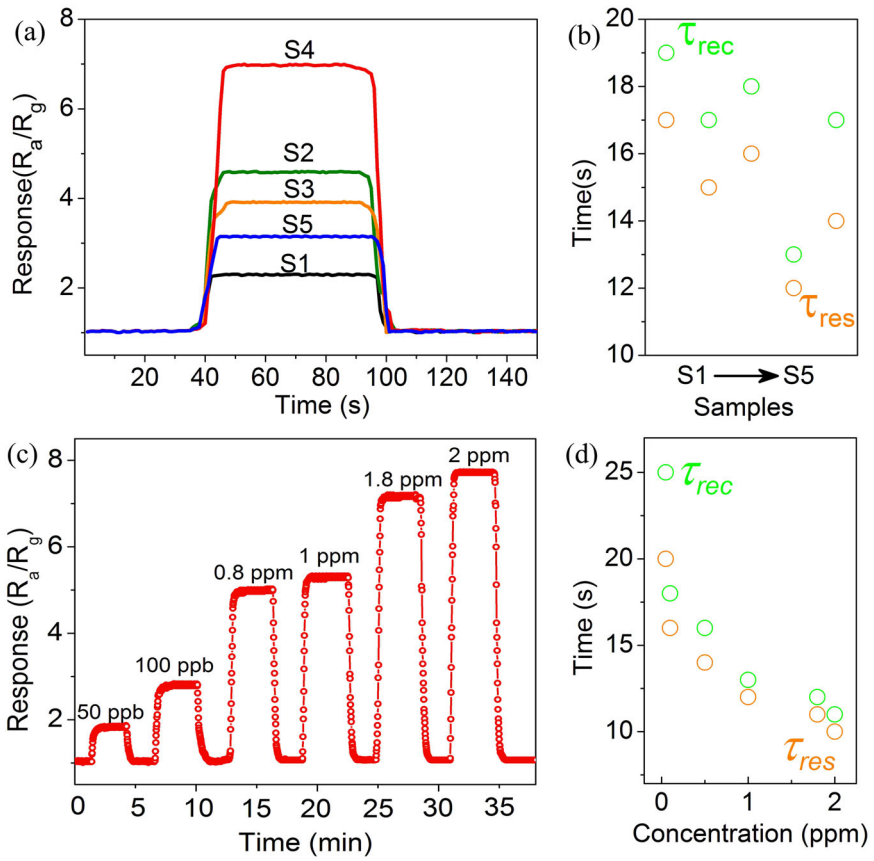

Fig. 5 a Dynamic responses of the S1–S5 NW gas sensors to 1.8 ppm acetone at their optimal operating temperature (390, 380, 350, 320, and 340 °C, respectively) and **b** their corresponding τ_{res} and τ_{rec}. **c** Dynamic responses of the S4 Pt@In_2O_3 core-shell NW gas sensor to different acetone concentrations at 320 °C and **d** its corresponding τ_{res} and τ_{rec}

slightly, demonstrating the good cross-selectivity of the S4 Pt@In_2O_3 core-shell NW sensor. To verify the stability of the as-prepared gas sensors, the long-term stability is checked every 5 days for 1 month. As shown in Fig. 6b, the stability of the sensors based on the Pt@In_2O_3 core-shell NWs is much better than that of the mixed one (S2 sensor), especially that of the S4 Pt@In_2O_3 core-shell NW sensor, thereby further confirming its good sensing properties.

Moisture is one of the crucial influencing factors that must be considered regarding practical use because of the high humidity in the exhaled breath environment. As already known, the response of gas sensors based on SMOs is easily influenced by a high RH% condition. Herein, we further introduce an additional moisture filter layer by using SBA-15 to cover the Pt@In_2O_3 core-shell NW sensing layer (Fig. 7a). Note that SBA-15 is a kind of mesoporous silica molecular sieve with a specific pore channel from top to bottom. Moreover, the pore size of the SBA-15 molecular sieve (9 nm, Supplementary Fig. S8) is much larger than the diameter of an acetone molecule (0.469 nm)[46], which ensures that acetone molecules can easily pass through it. In addition, it has been proven that the SBA-15 molecular sieve is an effective dessicant[47]. As illustrated in Fig. 7a, at a high operating temperature, the hydrolysis of siloxane bonds on the surface of amorphous walls of mesoporous silica may occur because of moisture, yielding silicon hydroxyl bonds, while in a dry environment, the silicon hydroxyl bonds may further condense back to siloxane bonds[48]. Thus, this sieve could be a good candidate for moisture gas filtering and for effectively maintaining the advantage of nanodevices, namely, their miniaturized scale. As shown in Fig. 7b, c, the cross-sensitivity is defined as $R_{RH}/R_{g,RH}$, where R_{RH} is the resistance of the gas sensor in different RH% environments and $R_{g,RH}$ is the resistance of the gas sensor to 1.8 ppm of acetone in different RH% environments. First, the cross-sensitivity values obtained with only a sensitive NW layer are studied under different RHs (25 ~ 100%). The sensor responses decrease quickly from 6.9 to 2.3 as the RH% increases from 25 to 100% (Fig. 7b). This mainly occurs because large concentrations of moisture molecules partially occupy the active surface of the sensitive layer and deteriorate the sensor's response to acetone.

Table 1 Results from recent publications on chemical resistance sensors based on SMOs for detecting acetone gas in different humidity environments and comparison with the properties of the S4 Pt@In_2O_3 core-shell NW sensor developed in this work

Sensing materials	Response	Response in this work	Detection limit	Testing environment	Operating temperature	Response /recovery time	References
Co-doped ZnO nanofibers	16 at 100 ppm	——	5 ppm	25% RH	360 °C	——	55
In_2O_3-coated CeO_2 nanoclusters	4.46 at 20 ppm	47 at 20 ppm	500 ppb	80% RH	450 °C	16 s/ 117 s	56
Zn_3N_2/ZnO hollow microspheres	21.2 at 20 ppm	47 at 20 ppm	70 ppb	90% RH	200 °C	15 s/ 27 s	57
Pt-WO_3 hemitube	4.11 at 2 ppm	6.92 at 2 ppm	120 ppb	85% RH	300 °C	>60 s/ >60 s	58
Pt-doped SnO_2 NFs	7.12 at 3 ppm	10.3 at 3 ppm	25 ppb	80% RH	300 °C	>60 s/ >60 s	1
Au/1D α-Fe_2O_3	5.91 at 1 ppm	6.23 at 1 ppm	≤1 ppm	45% RH	270 °C	15 s/ 20 s	59
Si-doped WO_3	2.5 at 0.6 ppm	4.5 at 0.6 ppm	20 ppb	90% RH	400 °C	95 s/ 80 s	60
S4 Pt@In_2O_3 NWs	6.23 at 1 ppm	6.23 at 1 ppm	10 ppb	~100% RH	320 °C	11 s/ 13 s	This work

Figure 7c shows the responses of the sensors after introducing the moisture filter layer under the same condition. Different from Fig. 7b, the responses of the gas sensors change only slightly. The result confirms that the molecular sieve layer can effectively decrease the influence of moisture, even in a high RH% environment.

Based on the above sensing analysis, clinical detection is further carried out to test the sensing performance of the S4 Pt@In_2O_3 core-shell NW sensor with respect to human breath samples. To make the data more representative, the breath samples are taken from 30 diabetic patients and 13 healthy volunteers. Supplementary Fig. S9 shows the enlarged response distribution diagram of the S4 Pt@In_2O_3 core-shell NW gas sensor before and after application of the molecular sieve when analyzing real breath samples exhaled by healthy volunteers. Because the surface active sites of the sensors are under high humidity, the response values range from 1.0–1.4 for healthy volunteers before the molecular sieve layer is used. After introducing the moisture filter layer, the corresponding range becomes broader and higher (1.6–2.4). This demonstrates that the molecular sieve layer is very helpful in reducing the interference due to humidity. Furthermore, as shown in Fig. 7d, the sensor with only a sensitive NW layer can well distinguish between diabetic patients and healthy people but with a much lower response than the experimental data. After the introduction of the moisture filter layer (Fig. 7e), all the response values become approximately threefold higher than those under the untreated conditions, and the difference in response between diabetic and healthy volunteers becomes more obvious. This further proves the advantage of the anti-interference properties with respect to RH% of the as-prepared sensor with the moisture filter layer. In addition, cross-sectional SEM images of the sensor without or with a moisture filter layer are shown in the insets of Fig. 7d, e, respectively. The thicknesses of the sensitive layer and moisture filter layer are approximately 20 and 30 μm, respectively.

Considering that the hydrolysis of siloxane bonds in SBA-15 can lead to the destruction of the mesopores in SBA-15, the stability of the S4 Pt@In_2O_3 core-shell NW gas sensor coated with the SBA-15 molecular sieve should be carefully investigated. Supplementary Fig. S10a shows the short-term and the long-term stability of the sensor in the presence of the breath exhaled by the healthy volunteers with 1.8 ppm of acetone added. The short-term stability is obtained by measuring the target gas five times, which reveals its good reproducibility. Supplementary Fig. S10b shows the long-term stability of the S4 Pt@In_2O_3 core-shell NW gas sensor coated with the molecular sieve. After 30 days, the sensor still maintains 90% of the original value, indicating its good long-term stability. In addition, small-angle XRD and nitrogen

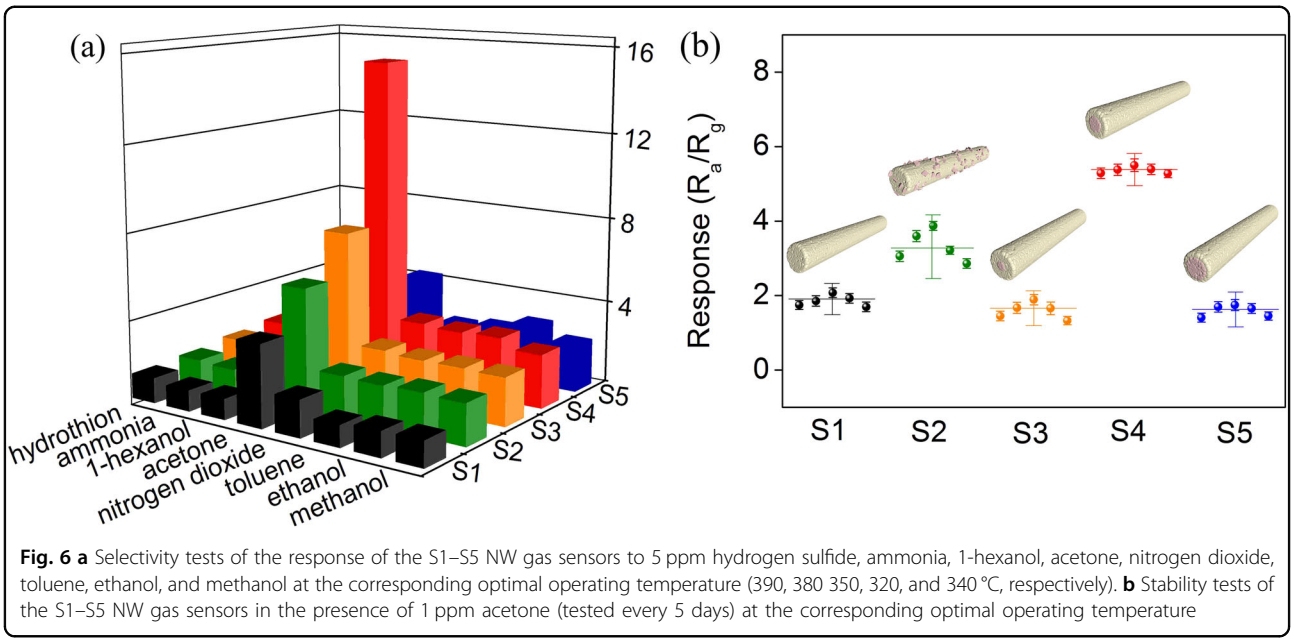

Fig. 6 a Selectivity tests of the response of the S1–S5 NW gas sensors to 5 ppm hydrogen sulfide, ammonia, 1-hexanol, acetone, nitrogen dioxide, toluene, ethanol, and methanol at the corresponding optimal operating temperature (390, 380 350, 320, and 340 °C, respectively). **b** Stability tests of the S1–S5 NW gas sensors in the presence of 1 ppm acetone (tested every 5 days) at the corresponding optimal operating temperature

adsorption–desorption isotherm experiments are conducted to further evaluate the stability of SBA-15 from the viewpoint of structure. Supplementary Fig. S10c compares the small-angle XRD patterns of pristine SBA-15 and SBA-15 treated 50 and 100 times with breath exhaled by healthy volunteers. All the SBA-15 samples present the (100), (110), and (200) lattice planes associated with the well-ordered hexagonal symmetry array of a mesoporous structure, and the intensities of the diffraction peaks undergo little change, indicating that the uniformity of SBA-15 does not decrease after multiple expiratory treatments. This can be further confirmed via a N_2 adsorption–desorption isotherm measurement (Supplementary Fig. S10d), which is performed to monitor the condition of the mesoporous structure of SBA-15 after exposure to the exhalation process. Pristine SBA-15 and SBA-15 treated 50 and 100 times with breath exhaled by healthy volunteers have calculated specific surface areas of 569, 532, and 512 $m^2 g^{-1}$ and total pore volumes of 0.745, 0.699, and 0.576 $cm^3 g^{-1}$, respectively. According to the comparison, after 50 and 100 expiratory treatments, 93.5% and 90% of the original values of the specific surface areas can be maintained, whereas 93.8% and 77.3% of the original total pore volume values can be maintained, respectively. The small reduction in the surface area and pore volume can be attributed to the partial structural collapse after a certain number of iterations of the expiratory process, indicating that the SBA-15 filter layer can still retain favorable stability even after 100 expiratory treatments.

Herein, to further confirm the practicality of the as-prepared S4 Pt@In_2O_3 core-shell NW sensor with the moisture filter layer, we place it inside a simple portable sensing device designed by us to perform real-time measurements of some healthy and diabetic volunteers. As shown in Fig. 8a, the moisture filter layer can trap water molecules, while the acetone biomarkers can pass through the pores of SBA-15. During testing, the volunteers continually blew into the air intake of the portable sensing device for 2 s. When the S_m value is lower than 5.5 (the case of a healthy volunteer, Fig. 8b), the portable sensing device will display "normal"; otherwise, it will display "high value" (the case of a diabetic volunteer, Fig. 8c). We also made a video to record real-time measurements of some healthy and diabetic volunteers (Supporting Information Video). The result is consistent with that shown in Fig. 8, further confirming the high-performance of the as-prepared sensor even when used in a simple portable sensing device. It should be mentioned that the portable sensing device exhibited a faster dynamic process than the sensors without SBA-15. This can be attributed to the different test environments of these two kinds of sensors. As shown in the video, the volunteers blew into the air intake of the portable sensing device. This process can provide additional force that drives air movement, thereby making the target gas reach the sensitive layer more quickly. When the sensors without SBA-15 were tested under a static process, the resistance value needed a relatively longer time to reach the final stable status. Therefore, the response time of the portable sensing device is faster than that of the sensors without SBA-15.

Gas sensing mechanism of Pt@In_2O_3 sensors

To better understand the gas sensing characteristics of the Pt@In_2O_3 core-shell NWs, the sensing mechanism is further examined. First, based on the nanostructure, the

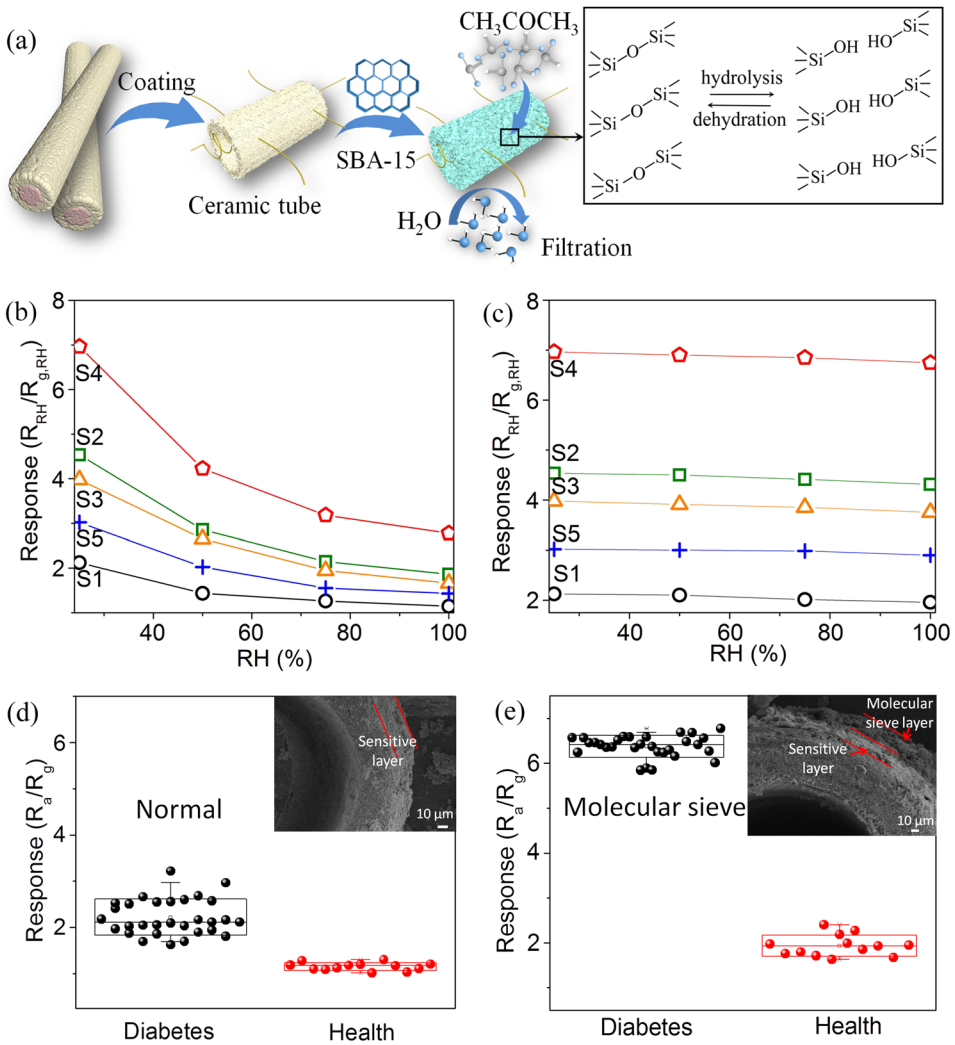

Fig. 7 a Schematic illustration of the hydrolysis and dehydration process of a molecular sieve. **b** The response of the S1–S5 NW gas sensors (1.8 ppm) as function of RH% and **c** the response of the S1–S5 NW gas sensors after coating with a molecular sieve layer (SBA-15) as function of RH%. **d** The responses of the S4 gas sensor and **e** the response of the S4 gas sensor coated with the molecular sieve layer to real exhaled breath samples from diabetic and healthy volunteers. The insets are SEM images of gas sensors before (**d**) and after (**e**) coating with the molecular sieve layer

mechanism could be consistent with the sensing mechanism of typical n-type SMO gas sensors. Briefly, this sensing mechanism involves resistance changes induced by the chemisorption of oxygen ions (O_2^-, O^-, and/or O^{2-}), which can interact with reducing gases (acetone in our case), thereby modifying the surface depletion region and the sensor resistance[40]. Upon exposure of the surface to gaseous acetone, the acetone gas molecules react with the adsorbed oxygen ions and release electrons to the In_2O_3 surface, resulting in an increase in electron concentration and a decrease in resistance. This reaction can be expressed as:

$$CH_3COCH_{3(gas)} + 8O^{2-} \rightarrow 3CO_{2(gas)} + 3H_2O_{(gas)} + 8e^- \quad (1)$$

Based on this mechanism, the increased sensing properties of Pt@In_2O_3 core-shell NWs can be considered from the following aspects. First, the change in resistance is the most important factor, as it can directly influence the sensing response in the absorption-desorption mechanism. Since the oxygen adsorption and the corresponding sensing reaction with respect to acetone mainly occur on the surface of the sensitive material, the decrease in inner resistance can effectively enlarge the change in surface resistance. To prove this hypothesis, we further demonstrate the response to a reducing gas based on an n-type SMO as:

$$Response = \frac{R_{in} + R_a'}{R_{in} + R_g'}, \quad (2)$$

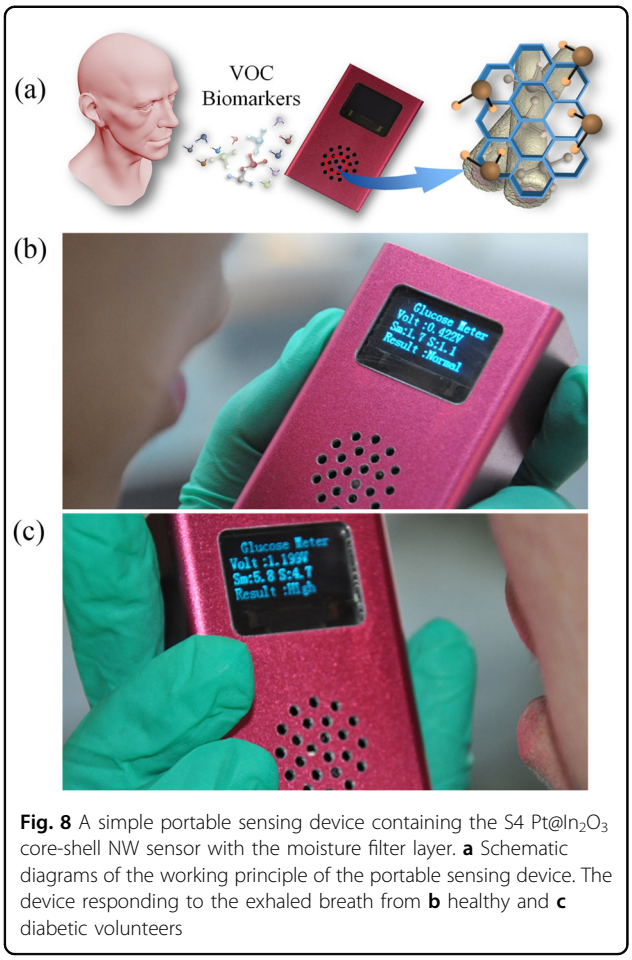

Fig. 8 A simple portable sensing device containing the S4 Pt@In_2O_3 core-shell NW sensor with the moisture filter layer. **a** Schematic diagrams of the working principle of the portable sensing device. The device responding to the exhaled breath from **b** healthy and **c** diabetic volunteers

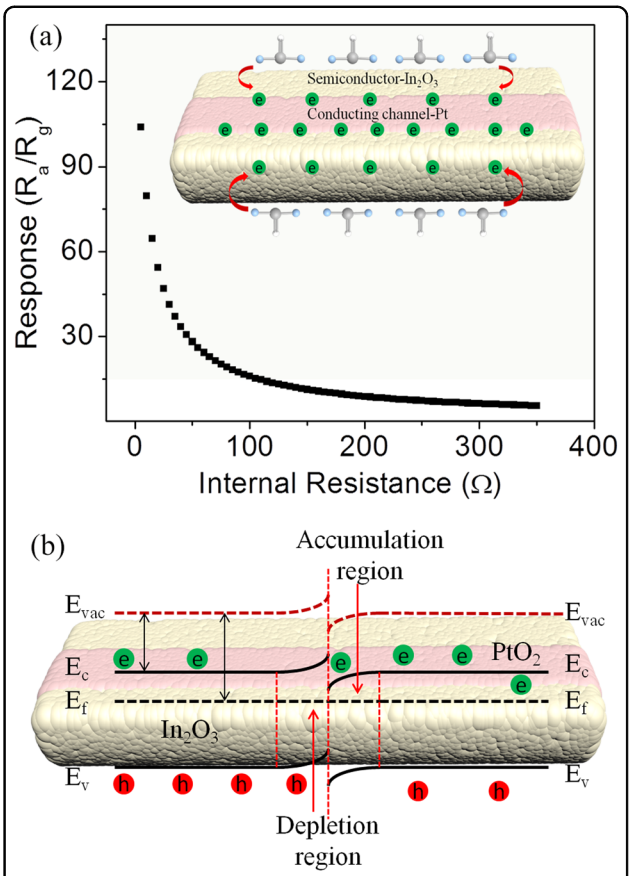

Fig. 9 a The relationship between the ratio of R_a'/R_g', and R_{in}. The inset displays schematic diagrams showing the electron density forming at In_2O_3 and the conducting channel Pt junction upon exposure to acetone gas. **b** The schematic diagram of the p–n heterojunction between In_2O_3 and PtO_2. (E_{vac} = valence band edge energy, E_c = conduction band edge energy, E_f = Fermi level)

where R_{in} is the inner resistance of the n-type semiconductor, which will not change either in air or in the target gas; R_a' is the surface resistance in air; and R_g' is the surface resistance in the target gas. As calculated in Fig. 9a, the relationship between the ratio R_a'/R_g' and R_{in} obeys a reduced power function model. That is, when the internal resistance decreases, the change in the surface resistance after exposure to the target gas is considerably amplified. This indicates that the response in a similar sensing system can be further optimized by decreasing the value of R_{in}. Considering this result together with the EIS results presented in Fig. 4a, the conductivity of the Pt core is very good; hence, compared to the pure In_2O_3 NWs and even the Pt/In_2O_3 mixed NWs, the S4 Pt@In_2O_3 core-shell NW sample exhibits much better sensing behavior with respect to the target gas (inset of Fig. 9a). This can be further extended to the response of the S3 Pt@In_2O_3 core-shell NW sensor: the R_{in} value is not an optimized one due to the thinner and discontinuous Pt core, and thus, it has a lower response than the S4 Pt@In_2O_3 core-shell NW sensor. The response decreases further for the S5 Pt@In_2O_3 core-shell NW sensor, which contains a continuous Pt core with a larger diameter. This result may have occurred because there is not enough sensitive material to adsorb the abundant oxygen ions during the reaction with the target gas.

On the other hand, the Pt core may be partly converted to PtO_2 when exposed to oxygen at elevated temperatures; this can be proved by the XPS spectra (Fig. 3d). Generally, PtO_2 exhibits the p-type semiconductor property with a work function of 5.65 eV[49], which is opposite to that of the n-type In_2O_3 (5.0 eV)[50]. Thus, p–n junctions can be formed along the interface between the outer shell (In_2O_3) and the inner core. These results are verified by the Mott–Schottky analysis shown in Fig. 4b, and the corresponding schematic band diagrams of the In_2O_3–PtO_2 heterojunction are displayed in Fig. 9b. As the position of the Fermi level in In_2O_3 is higher than that of PtO_2, electron transfer occurs from In_2O_3 to PtO_2 via band bending until the system achieves equalization at the Fermi level, leading to a wide depletion of layers, and a potential barrier is established. As a result, the formation of the p–n junction causes a high-resistance state in the air.

Table 2 Cross-selectivity test of the S4 Pt@In_2O_3 core-shell NW sensor with 5 ppm interfering gases in the presence of 5 ppm acetone

Gas species	Response of S4 sensor
5 ppm acetone	15.21
5 ppm acetone + 5 ppm hydrogen sulfide	15.84
5 ppm acetone + 5 ppm ammonia	15.63
5 ppm acetone + 5 ppm 1-hexanol	16.07
5 ppm acetone + 5 ppm nitrogen dioxide	15.41
5 ppm acetone + 5 ppm toluene	16.04
5 ppm acetone + 5 ppm ethanol	16.00
5 ppm acetone + 5 ppm methanol	15.68

Regarding the selectivity mechanism, this complex process is difficult to understand and has yet to be clarified, as it depends on many factors, such as the operating temperature, the rate of gas diffusion or the chemical reaction at the surface, the physical preparation of the sensor material, the Debye length, and the charge carrier concentration[51–54]. In this study, all the gas sensing tests were performed at the optimum operating temperature for acetone gas for each kind of sensor. According to Supplementary Fig. S11 (taking the S4 Pt@In_2O_3 core-shell NW sensor as an example), the optimum operating temperatures for the other gases are not the same as that for acetone (320 °C); that is, the activation energy of the related reactions is not sufficient at this temperature for the other interfering gases. This may partially explain the reason why the sensors had a high sensitivity for acetone over the other tested gases.

Conclusions

In summary, we have presented a highly sensitive and humidity-resistant sensor comprising Pt@In_2O_3 core-shell NW sensitive layers and a parallel SBA-15 molecular sieve moisture filter layer. The Pt@In_2O_3 core-shell NWs were fabricated using a simple co-electrospinning method, which yielded a porous In_2O_3 shell and a controllable Pt core with high conductivity. Due to the rational design of these materials, the S4 Pt@In_2O_3 core-shell NWs showed enhanced sensing properties in the presence of a low acetone concentration, demonstrating an up to sixfold increase in the sensing response compared to that of pure In_2O_3 NWs. It demonstrated a low detection limit of 10 ppb, short τ_{res} and τ_{rec} of 14 and 16 s for 1 ppm of acetone, and high selectivity and stability. In addition, when the SBA-15 moisture filter layer was introduced, highly accurate information could be obtained during clinical sample testing, such as an improved response difference between breath samples obtained from healthy people and people with diabetes. This work shows that this well-engineered sensor structure can function as an ultrasensitive sensing platform for the real-time detection of diabetes biomarkers in exhaled breath. More importantly, this work demonstrates an example of a simple and versatile method for increasing the ability to neutralize the interference due to humidity while simultaneously maintaining the miniaturized scale of nanodevices. We believe that this method can be used in the design of other gas sensors and can serve as an economical yet powerful tool for developing portable and flexible sensors.

Supporting information

Additional characterization and the synthesis of pure In_2O_3 NWs and Pt/In_2O_3 NWs; EDX analysis of Pt/In_2O_3 NWs; the process of sampling exhaled breath; the size distribution, grain size statistics, and XRD patterns of samples S1–S5; the wall thicknesses of samples S3–S5; the response of gas sensors S1–S5 to different acetone concentrations; additional TEM images of the SBA-15 molecular sieve; the enlarged response figure for the Pt@In_2O_3 sensor; small-angle XRD and Brunauer-Emmett-Teller (BET) isotherm characterization of SBA-15; the operating temperatures of sensors S1–S5 for 10 ppm of acetone and that of sensor S4 for 5 ppm of hydrogen sulfide, ammonia, 1-hexanol, methanol, ethanol, toluene, and NO_2; additional tables listing the SBA-15 specifications and the clinical data corresponding to the tested volunteers; a table presenting the details regarding the binding energy of deficient oxygen, adsorbed oxygen, and OH groups and the impedance values; fitted data regarding the resistances of NW samples S1–S5 obtained via EIS.

Acknowledgements
This work was supported by the National Key Research and Development Program (2016YFC0207101), the Jilin Province Natural Science Foundation of China (No. 20150520090JH, 20170520129JH, and 20170520111JH), the Major State Basic Research Development Program of China (973 Program) (No. 2014CB643506), the program of Chang Jiang Scholars and Innovative Research Team in University (No. IRT13018) and the National Natural Science Foundation of China (Grant no. 21403084 and 11674127).

Conflict of interest
The authors declare that they have no conflict of interest.

Supplementary information is available for this paper at https://doi.org/10.1038/s41427-018-0029-2.

Received: 24 September 2017 Revised: 4 January 2018 Accepted: 17 January 2018.
Published online: 17 April 2018

References

1. Jang, J. -S., Choi, S. -J., Kim, S. -J., Hakim, M. & Kim, I. -D. Rational design of highly porous SnO_2 nanotubes functionalized with biomimetic nanocatalysts for direct observation of simulated diabetes. *Adv. Funct. Mater.* **26**, 4740–4748 (2016).
2. Parkes, J. L., Slatin, S. L., Pardo, S. & Ginsberg, B. H. A new consensus error grid to evaluate the clinical significance of inaccuracies in the measurement of blood glucose. *Diabetes Care* **23**, 1143–1148 (2000).
3. Storer, M. et al. Measurement of breath acetone concentrations by selected ion flow tube mass spectrometry in type 2 diabetes. *J. Breath. Res.* **5**, 046011 (2011).
4. Kahn, N., Lavie, O., Paz, M., Segev, Y. & Haick, H. Dynamic nanoparticle-based flexible sensors: diagnosis of ovarian carcinoma from exhaled breath. *Nano Lett.* **15**, 7023–7028 (2015).
5. Yi, W. Y. et al. A survey of wireless sensor network based air pollution monitoring systems. *Sensors* **15**, 31392–31427 (2015).
6. Henriksson, J., Villanueva, L. G. & Brugger, J. Ultra-low power hydrogen sensing based on a palladium-coated nanomechanical beam resonator. *Nanoscale* **4**, 5059–5064 (2012).
7. Zhang, J., Liu, X., Neri, G. & Pinna, N. Nanostructured materials for room-temperature gas sensors. *Adv. Mater.* **28**, 795–831 (2016).
8. Song, Z. et al. Sensitive room-temperature H_2S gas sensors employing SnO_2 quantum wire/reduced graphene oxide nanocomposites. *Chem. Mater.* **28**, 1205–1212 (2016).
9. Shehada, N. et al. Ultrasensitive silicon nanowire for real-world gas sensing: noninvasive diagnosis of cancer from breath volatolome. *Nano Lett.* **15**, 1288–1295 (2015).
10. Zhang, L. et al. Novel Mn_3O_4 micro-octahedra: promising cataluminescence sensing material for acetone. *Chem. Mater.* **21**, 5066–5071 (2009).
11. Saetia, K. et al. Spray-layer-by-layer carbon nanotube/electrospun fiber electrodes for flexible chemiresistive sensor applications. *Adv. Funct. Mater.* **24**, 492–502 (2014).
12. Silva, L. et al. Acetone gas sensor based on α-Ag_2WO_4, nanorods obtained via a microwave-assisted hydrothermal route. *J. Alloy. Compd.* **683**, 186–190 (2016).
13. Wang, L. L., Dou, H. M., Lou, Z. & Zhang, T. Encapsuled nanoreactors (Au@SnO_2): a new sensing material for chemical sensors. *Nanoscale* **5**, 2686–2691 (2013).
14. Arnal, P. M., Comotti, M. & Schüth, F. High-temperature-stable catalysts by hollow sphere encapsulation. *Angew. Chem., Int. Ed.* **45**, 8224–8227 (2006).
15. Subramanian, V., E. E., W. & P. V., K. Influence of metal/metal ion concentration on the photocatalytic activity of TiO_2-Au composite nanoparticles. *Langmuir* **19**, 469–474 (2003).
16. Konvalina, G. & Haick, H. Effect of humidity on nanoparticle-based chemiresistors: a comparison between synthetic and real-world samples. *ACS Appl. Mater. Interfaces* **4**, 317–325 (2012).
17. Zilberman, Y., Ionescu, R., Feng, X., Muellen, K. & Haick, H. Nanoarray of polycyclic aromatic hydrocarbons and carbon nanotubes for accurate and predictive detection in real-world environmental humidity. *ACS Nano.* **5**, 6743–6753 (2011).
18. Nishibori, M., Shin, W., Izu, N., Itoh, T. & Matsubara, I. Sensing performance of thermoelectric hydrogen sensor for breath hydrogen analysis. *Sens. Actuators, B.* **137**, 524–528 (2009).
19. Mondal, S. P. et al. Development of high sensitivity potentiometric NO_x sensor and its application to breath analysis. *Sens. Actuators, B.* **158**, 292–298 (2011).
20. Mane, G. P. et al. Preparation of highly ordered nitrogen-containing mesoporous carbon from a gelatin biomolecule and its excellent sensing of acetic acid. *Adv. Funct. Mater.* **22**, 3596–3604 (2012).
21. Xing, R. et al. Au-modified three-dimensional In_2O_3 inverse opals: synthesis and improved performance for acetone sensing toward diagnosis of diabetes. *Nanoscale* **7**, 13051–13060 (2015).
22. Xu, L. et al. Electrospinning preparation and room temperature gas sensing properties of porous In_2O_3 nanotubes and nanowires. *Sens. Actuators, B.* **147**, 531–538 (2010).
23. Kuribayashi, K. & Kitamura, S. Preparation of Pt-PtO_x thin films as electrode for memory capacitors. *Thin Solid Films* **400**, 160–164 (2001).
24. Yang, D.-J., Kamienchick, I., Youn, D. Y., Rothschild, A. & Kim, I. -D. Ultrasensitive and highly selective gas sensors based on electrospun SnO_2 nanofibers modified by Pd loading. *Adv. Funct. Mater.* **20**, 4258–4264 (2010).
25. Zhen, Y. & Li, J. Abnormal grain growth and new core–shell structure in (K,Na)NbO_3-based lead-free piezoelectric ceramics. *J. Am. Ceram. Soc.* **90**, 3496–3502 (2007).
26. Wang, H. -Q., Wu, Z. -B., Liu, Y. & Wang, Y. -J. Influences of various Pt dopants over surface platinized TiO_2 on the photocatalytic oxidation of nitric oxide. *Chemosphere* **74**, 773–778 (2009).
27. Cho, K. -C., Hwang, K. -C., Sano, T., Takeuchi, K. & Matsuzawa, S. Photocatalytic performance of Pt-loaded TiO_2 in the decomposition of gaseous ozone. *J. Photochem. Photobiol., A.* **161**, 155–161 (2004).
28. Shin, J. et al. Thin-wall assembled SnO_2 fibers functionalized by catalytic Pt nanoparticles and their superior exhaled-breath-sensing properties for the diagnosis of diabetes. *Adv. Funct. Mater.* **23**, 2357–2367 (2013).
29. Wang, D., Peng, Q. & Li, Y. Nanocrystalline intermetallics and alloys. *Nano Res.* **3**, 574–580 (2010).
30. Chen, C., Ma, W. & Zhao, J. Semiconductor-mediated photodegradation of pollutants under visible-light irradiation. *Chem. Soc. Rev.* **39**, 4206–4219 (2010).
31. Xiong, L., Yang, X., Xu, M., Xu, Y. & Wu, D. Pt–Ni alloy nanoparticles supported on multiwalled carbon nanotubes for methanol oxidation in alkaline media. *J. Solid State Electrochem.* **17**, 805–810 (2013).
32. Cai, J., Li, S., Pan, H., Liu, Y. & Qin, G. c-In_2O_3/α-Fe_2O_3 heterojunction photoanodes for water oxidation. *J. Mater. Sci.* **51**, 8148–8155 (2016).
33. Dervisevic, M., Senel, M., Sagir, T. & Isik, S. Boronic acid vs. folic acid: A comparison of the bio-recognition performances by impedimetric cytosensors based on ferrocene cored dendrimer. *Biosens. Bioelectron.* **91**, 680–686 (2017).
34. Shi, W., Zhu, J., Sim, D., Tay, Z. & Yan, Q. Achieving high specific charge capacitances in Fe_3O_4/reduced graphene oxide nanocomposites. *J. Mater. Chem.* **21**, 3422–3427 (2011).
35. Wolcott, A., Smith, W. A., Kuykendall, T. R., Zhao, Y. & Zhang, J. Z. Photoelectrochemical water splitting using dense and aligned TiO_2 nanorod arrays. *Small* **5**, 104–111 (2009).
36. Hakiki, N. B., Boudin, S., Rondot, B. & Belo, M. D. C. The electronic structure of passive films formed on stainless steels. *Corros. Sci.* **37**, 1809–1822 (1995).
37. Pan, L. et al. Constructing TiO_2 p-n homojunction for photoelectrochemical and photocatalytic hydrogen generation. *Nano Energy* **28**, 296–303 (2016).
38. Chen, Y. et al. A CuO–ZnO nanostructured p–n junction sensor for enhanced N-butanol detection. *RSC Adv.* **6**, 2504–2511 (2016).
39. Basu, P. K., Kallatt, S., Anumol, E. A. & Bhat, N. Suspended core-shell Pt-PtO_x nanostructure for ultrasensitive hydrogen gas sensor. *J. Appl. Phys.* **117**, 224501 (2015).
40. Xu, S. et al. Role of the heterojunctions in In_2O_3-composite SnO_2 nanorod sensors and their remarkable gas-sensing performance for NO_x at room temperature. *Nanoscale* **7**, 14643–14651 (2015).
41. Kim, S. et al. Enhanced acetone gas sensing performance of the multiple-networked Fe_2O_3-functionalized In_2O_3 nanowire sensor. *Curr. Appl. Phys.* **15**, 947–952 (2015).
42. Kim, S. et al. Significant enhancement of the sensing characteristics of In_2O_3 nanowires by functionalization with Pt nanoparticles. *Nanotechnology* **21**, 415502 (2010).
43. Mastrigt, E., Jongste, J. & Pijnenburg, M. The analysis of volatile organic compounds in exhaled breath and biomarkers in exhaled breath condensate in children–clinical tools or scientific toys? *Clin. Exp. Allergy* **45**, 1170–1188 (2015).
44. Mudalel, M. L. et al. Mo1014 a high protein challenge increases gut-derived exhaled breath ammonia. *Gastroenterology* **146**, 986 (2014).
45. Hakim, M. et al. Volatile organic compounds of lung cancer and possible biochemical pathways. *Chem. Rev.* **112**, 5949–5966 (2012).
46. Nayak, A., Ghosh, R., Santra, S., Guha, P. & Pradhan, D. Hierarchical nanostructured WO_3–SnO_2 for selective sensing of volatile organic compounds. *Nanoscale* **7**, 12460–12473 (2015).
47. Serrano, D. P., Calleja, G., Botas, J. A. & Gutierrez, F. J. Adsorption and hydrophobic properties of mesostructured MCM-41and SBA-15 materials for VOC removal. *Ind. Eng. Chem. Res.* **43**, 7010–7018 (2004).
48. Zhang, F. Q. et al. Understanding effect of wall structure on the hydrothermal stability of mesostructured silica SBA-15. *J. Phys. Chem. B.* **109**, 8723–8732 (2005).
49. Cola, A. & Farella, I. The polarization mechanism in CdTe schottky detectors. *Appl. Phys. Lett.* **94**, 102113 (2009).
50. Wang, Q. et al. Synthesis and field-emission properties of In_2O_3 nanostructures. *Mater. Lett.* **62**, 2710–2713 (2008).
51. Fort, A. et al. Selectivity enhancement of SnO_2 sensors by means of operating temperature modulation. *Thin Solid Films* **418**, 2–8 (2002).
52. Mizsei, J. How can sensitive and selective semiconductor gas sensors be made? *Sens. Actuators, B.* **23**, 173–176 (1995).

53. Lee, A. P. & Reedy, B. J. Temperature modulation in semiconductor gas sensing. *Sens. Actuators, B.* **60**, 35–42 (1999).
54. Kim, H. J. & Lee, J. H. Highly sensitive and selective gas sensors using p-type oxide semiconductors: Overview. *Sens. Actuators, B.* **192**, 607–627 (2014).
55. Liu, L. et al. Improved selective acetone sensing properties of Co-doped ZnO nanofibers by electrospinning. *Sens. Actuators, B.* **155**, 782–788 (2011).
56. Yoon, J. W. et al. A new strategy for humidity independent oxide chemiresistors: Dynamic self-refreshing of In_2O_3 sensing surface assisted by layer-by-layer voated CeO_2 nanoclusters. *Small* **12**, 4229–4240 (2016).
57. Qu, F., Yuan, Y., Guarecuco, R. & Yang, M. Low working-temperature acetone vapor sensor based on zinc nitride and xxide hybrid composites. *Small* **12**, 3128–3133 (2016).
58. Choi, S. -J. et al. Selective diagnosis of diabetes using Pt-functionalized WO_3 hemitube networks as a sensing layer of acetone in exhaled breath. *Anal. Chem.* **85**, 1792–1796 (2013).
59. Gunawan, P. et al. Ultrahigh sensitivity of Au/1D alpha-Fe_2O_3 to acetone and the sensing mechanism. *Langmuir* **28**, 14090–14099 (2012).
60. Righettoni, M., Tricoli, A. & Pratsinis, S. E. Si: WO_3 sensors for highly selective detection of acetone for easy diagnosis of diabetes by breath analysis. *Anal. Chem.* **82**, 3581–3587 (2010).